High Heat Flux Tests in Support of the 3-D Computational Modeling of Melting for the EU-DEMO First Wall Limiters

M. L. Richiusa, H. Greuner, B. Böswirth, P. Ireland, and Z. Vizvary

***Abstract*— The EU-DEMOnstration fusion power plant (DEMO) first wall protection strategy relies on limiter components to face both normal and off-normal plasma transient events. The heat loads during these events are likely to damage the breeding blanket's first wall otherwise. Since W is the preferred plasma-facing material for EU-DEMO, the plasma-facing component design of the limiters follows considerations based on heat transfer in solids undergoing phase transition. The understanding of this problem has paved the way for a 1-D thermal modeling in MATLAB [Thermal Analysis foR Tracking InterFaces under meLting&vaporizaTion-induced plasma Transient Events (TARTIFL&TTE)], which has then been improved and extended to 3-D geometries within a Multiphysics environment. Hence, the 3-D TARTIFL&TTE implementation in COMSOL Multiphysics. Although the validation has already started against some data available in the literature and described in the companion paper, dedicated experiments are performed in the Garching LArge DIvertor Sample Test Facility (GLADIS) for melting studies. Carried out as a joint activity between EUROfusion and U.K. Atomic Energy Authority (UKAEA), the aim of these experiments is generating a traceable and controlled experimental database in support of heat transfer studies in solid components undergoing phase transition. The data are here used in support of the 3-D TARTIFL&TTE validation benchmark. To broaden the database, three different materials are chosen, i.e., TZM, W, and SS-316 grade. The requirements defining the experiments comply with the hypotheses behind 3-D TARTIFL&TTE, for it to be able to reproduce the experiments. Therefore, a uniform heat flux on the loaded surface is provided by the H neutral beam on the footprint, and loading time and heat flux magnitude are chosen such that only melting is reached. This allows the liquid metal to stay in place once formed. No attempts to reach vaporization are made, since the vertical position of the target promotes the molten layer sliding under gravity effects. Measured and modeled results (temperature, absorbed energy, and melt layer depth) show good agreement during the melting phase. As a stepwise benchmark, validation will be also sought under vaporization events. Future work is focused on addressing this last point.**

***Index Terms*— Design methodology, fusion power generation, tokamaks.**

NOMENCLATURE

Acronyms

DEMO	DEMOnstration fusion power plant.
GLADIS	Garching Large Divertor Sample Test Facility.
TARTIFL&TTE	Thermal Analysis foR Tracking InterFaces under meLting&vaporizaTion-induced plasma Transient Events.
UKAEA	U.K. Atomic Energy Authority.

Symbols

Cu	Copper.
E	Energy density [J m^{-2}].
FWHM	Full-width at half-maximum.
H	Hydrogen.
HF	Heat flux density [W·m^{-2}].
HTC	Heat transfer coefficient [W·m^{-2} K^{-1}].
IR	Infrared.
(1-2c) Pyro	(1-2 color) pyrometer.
SS	Stainless steel.
St.Dev.	Standard deviation [mm].
t	Time [s].
T	Temperature [°C].
TC, TC1, and TC2	Thermocouple.
Ti	Titanium.
TZM	Titanium–molybdenum–zirconium.
W	Tungsten.
Zr	Zirconium.

Subscripts

0	Initial and operational.
abs	Absorbed.
exp	Experimental.
load	Loading time.
m	Melting.
model	Modeled.
max	Maximum.
(1-2c) Pyro	(1-2 color) pyrometer.

Manuscript received 14 August 2023; revised 27 November 2023 and 16 January 2024; accepted 27 February 2024. This work was supported in part by the European Union through the Euratom Research and Training Programme within the framework of the EUROfusion Consortium under Grant 101052200 and in part by the Engineering and Physical Sciences Research Council (EPSRC) through the Henry Royce Institute for Advanced Materials under Grant EP/R00661X/1 and Grant EP/P021727/1. The review of this article was arranged by Senior Editor R. Chapman. *(Corresponding author: M. L. Richiusa.)*

M. L. Richiusa is with the Department of Engineering Science, Oxford Thermofluids Institute, University of Oxford, OX2 0ES Oxford, U.K., and also with UKAEA, Culham Campus, Abingdon, OX14 3DB Oxfordshire, U.K. (e-mail: lorena.richiusa@ukaea.uk).

H. Greuner and B. Böswirth are with the Max Planck Institute for Plasma Physics, 85748 Garching, Germany.

P. Ireland is with the Department of Engineering Science, Oxford Thermofluids Institute, University of Oxford, OX2 0ES Oxford, U.K.

Z. Vizvary is with UKAEA, Culham Campus, Abingdon, OX14 3DB Oxfordshire, U.K.

Color versions of one or more figures in this article are available at https://doi.org/10.1109/TPS.2024.3375642.

Digital Object Identifier 10.1109/TPS.2024.3375642

Greek

Ω_2 Dimensionless liquid variable [2].
Δ Difference [%].
ε Surface emissivity.
λ Wavelength [m].

I. Introduction

THE 3-D TARTIFL&TTE model tackling the phase transition occurrence when solid components are subjected to high HF is described in [2]. The 3-D TARTIFL&TTE is an FEM implementation through COMSOL Multiphysics and can be applied to 3-D domains undergoing nonuniform HF.

This article supports the 3-D TARTIFL&TTE validation against dedicated experimental results, whose primary aim is to test its capability of reliably predicting the molten layer depth. It includes the description of the melting experiments hosted by GLADIS (see Sections II–IV), the FEM model (Section V), the experimental results and related benchmark (Sections VI and VIII, respectively). Discussion on results and final conclusions are highlighted in Sections IX and X, respectively.

II. GLADIS Facility

The high HF test facility GLADIS is operated by the Max Plank Institute for Plasma Physics (Garching, Germany) [3]. It is equipped with two H neutral beam sources of 1 MW each, which generate almost homogeneous heating due to its nearly complete absorption onto the target surface. The 150-mm FWHM of the neutral beam deposits more than 90% of the central power density within a 50-mm-diameter footprint [3]. The comparison between the calorimetrically measured absorbed power and the calculated incident power is within a $\pm 5\%$ agreement. Therefore, all given HF and the resulting temperature data are within a scatter of 5%.

The following diagnostics are used for the experiments.

1) Beam calorimeter to measure the power density deposited onto the target.
2) One-color and two-color pyrometers, indicated, respectively, as 1c-Pyro [350 °C–3500 °C] and 2c-Pyro [500 °C–1700 °C].
3) The 200-Hz IR camera for surface temperature mapping.
4) Two n-type TCs at the back of the samples for in-depth temperature measurements up to 1700 °C.

The validation of the modeled data is based on the comparison against the following measured parameters, retrieved by combining both nondestructive and destructive postprocessing.

1) IR and 1c-Pyro surface temperature evolution, as well as TC temperature evolutions.
2) Integrated absorbed energy density.
3) Position of the solid-to-liquid interface at the end of the transient, measured through destructive postprocessing.

III. Sample Design, Fabrication, and Installation

The samples are 80 × 60 × 30 mm^3 sized bricks shown in Fig. 1. Two TCs are embedded in dedicated holes at different depths, i.e., 20 and 2 mm, respectively, at the back of the sample.

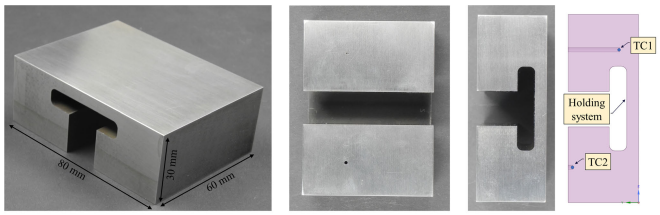

Fig. 1. From left to right: isometric, rear, and lateral views of the manufactured samples. An additional geometrical cross section highlighting the position of the TCs.

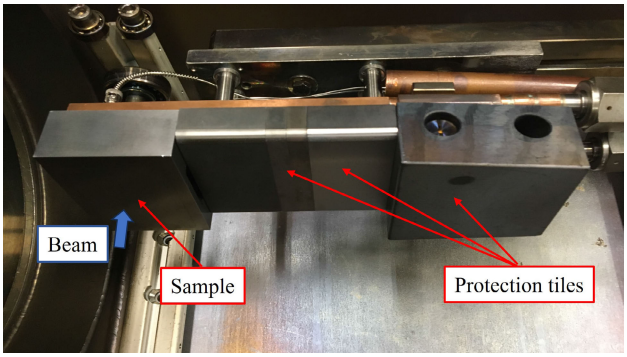

Fig. 2. Sample mounting and installation.

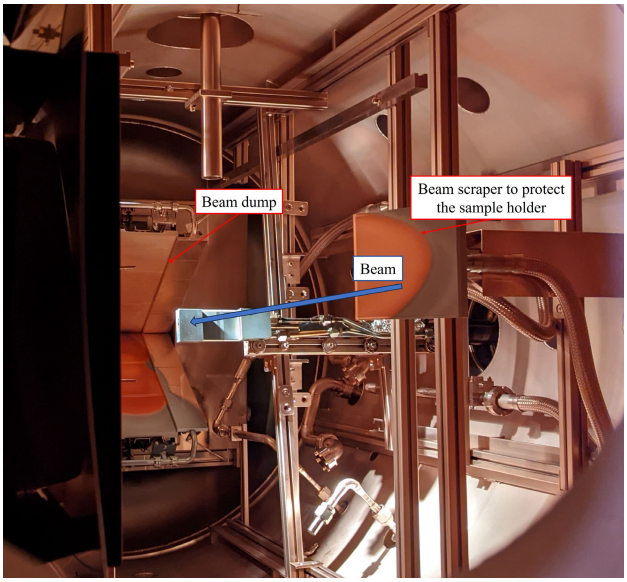

Fig. 3. Installation of the sample within the GLADIS main chamber.

Fig. 2 shows an overview of the sample installation before they are introduced into the main vacuum chamber. Fig. 3 shows the sample inserted in the main chamber and ready for the experiments.

The three materials listed below are selected, based on both their relevance to fusion components (i.e., W and TZM) and the possibility to broaden and diversify the database (SS-316). For every material, two samples are loaded for result repeatability.

TABLE I
SAMPLE'S EXPERIMENTAL PARAMETERS

Sample	HF_{max} [MW m^{-2}]	St.Dev. [mm]	Δt_{load} [s]	$t_{m,pyro}$ [s]	$t_{m,IR}$ [s]	T_0 [°C]
TZM-1	30	64.98	1.567	0.96	0.96	12
TZM-2			1.301	0.95	0.95	13
W-1	30	64.98	1.865	1.48	1.49	12
W-2			1.819	1.50	1.50	17
SS-1	10	64.64	1.875	1.61	1.61	19
SS-2			2.109	1.63	1.60	20

1) *TZM (TZM-1 and TZM-2 samples):* A 99.42%Mo alloy with 0.5%Ti and 0.08%Zr. It has the same thermal behavior than pure Mo but better mechanical properties, and a lower melting point than W.
2) *W (W-1 and W-2 Samples):* This is the targeted plasma-facing material for DEMO.
3) *SS-316 Grade (SS-1 and SS-2 Samples):* With its different behavior than TZM and W, SS helps diversify the experimental data.

The experimental setup foresees a horizontal beam focused on a vertical target; therefore, gravity acts on the molten layer that starts drifting down as soon as it appears. To comply with the TARTIFL&TTE assumption to have the liquid layer in place during the heating time, the exposure time is progressively calibrated in such a way to heat each target up to its melting point, hence minimizing any liquid layer loss under gravity. The heating time calibration starts after loading the first sample (TZM-1), which experiences the biggest mass loss under gravity, as shown in Sections IV and VI. Therefore, no attempts to reach vaporization is made.

IV. EXPERIMENTAL PARAMETERS

Every sample is thermally loaded under a spatial Gaussian HF distribution, whose maximum values and standard deviations are listed in Table I. For every sample, Table I reports the loading time, the time instants at which IR and 1c-Pyro trigger the beginning of the melting phase ($t_{m,IR}$ and $t_{m,pyro}$, respectively), and the initial temperature (T_0) calculated as the average value between the two TC measurements before the beam is switched on. Experiments are conducted under vacuum conditions.

V. FINITE-ELEMENT MODELING

The mesh is composed of 15 907 linear hexahedral elements, linked through 18 565 nodes. The variables the model solves for are temperature, mesh displacement, and surface deformation. The model is run within a deformed mesh domain, with material removal under evaporation and subsequent recession of the front face. Fig. 4 highlights the boundary conditions applied to the FEM. The Gaussian HF distribution is applied at the top surface [Fig. 4(a)]. The tile cooling is simulated by a convective condition at the back surface, with water flowing at T = 20 °C and providing HTC = 2000 W·m $^{-2}$K^{-1} [Fig. 4(b)]. The rest of the tile radiates energy toward the surrounding vessel at 20 °C [Fig. 4(c)], with temperature-dependent emissivity values. The emissivity of the molten surface is increased during the cooldown phase due to modifications in the surface morphology and finishing.

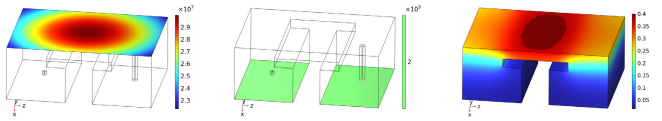

(a) (b) (c)

Fig. 4. FEM boundary conditions. (a) Spatial distribution of the HF [MW m^{-2}]. (b) Convective HTC value [W m^{-2} K^{-1}]. (c) T-dependent ε for W.

VI. THERMAL RESULTS FROM NONDESTRUCTIVE POSTPROCESSING

This section presents the modeled thermal results and their benchmark against the experimental data. For every materials' sample, dedicated subsections collect the related IR frames, the thermal benchmark against IR, Pyro, and TC temperature measurements, as well as the 3-D TARTIFL&TTE contour plots of the temperature distribution and the melt pool at the end of the heating time. Only one sample is shown per material. Considerations and conclusions are provided in Sections IX and X, respectively.

A. TZM—Temperature Data, Imaging, and Benchmark

This section reports the results related to TZM samples.

To better understand the gravity effect on the melt pool during a longer exposure time (already anticipated in Sections III and IV, the IR frames of both the TZM-1 and TZM-2 heat pulses are reported in Figs. 5 and 6, respectively.

As a general consideration valid for the temperature measurements shown in Fig. 7 and throughout the text (including Figs. 10 and 13 in Sections VI-B and VI-C, respectively), it is noted here that the deviation between IR and 1c-Pyro measurements beyond a certain threshold (≈2000 °C), is mainly based on the measurements at a different λ. The IR camera and the pyrometers work with fixed emissivity values, which do not completely consider the change of emissivity depending on sample temperature and energy (i.e., radiative wavelength). For W, in particular, ε depends strongly on the temperature and λ of the used optical devices.

Therefore, for compensating this variation in surface emissivity, IR and 1c-Pyro temperature measurements are extrapolated by adjusting their emissivity upon two certain data, i.e., the low-temperature 2c-Pyro temperature value and, at high temperature, the sudden change of emissivity at melting corresponding to the well-known melting temperature. The 2c-Pyro is used for measuring the reference emissivity value at low temperature threshold (below 1700 °C). This explains the mismatch between IR and 1c-Pyro data above 2000 °C. The IR and 1c-Pyro experimental temperature extrapolation is valid for all the heat pulses.

Both the 1c and 2c-Pyros can be used for temperature measurements up to 1700 °C. This is the maximum temperature threshold of the 2c-Pyro, beyond which it becomes insensitive. It starts acquiring temperature values when the sample cools down to 1700 °C, but at this point, the captured temperature values are unreliable because affected by different values of surface emissivity due to phase transition surface alterations.

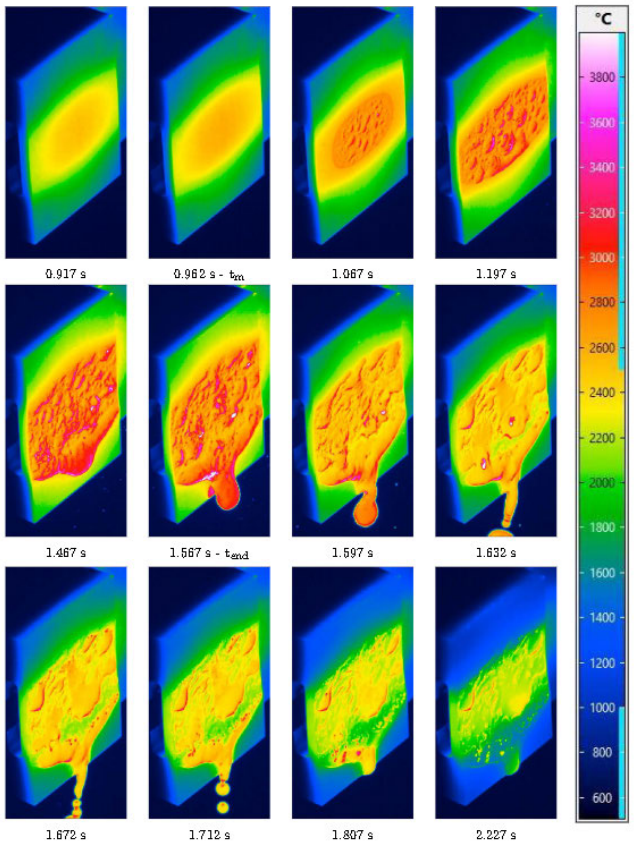

Fig. 5. TZM-1 IR frames showing the temperature and melt pool evolutions at different time instants during the heat pulse.

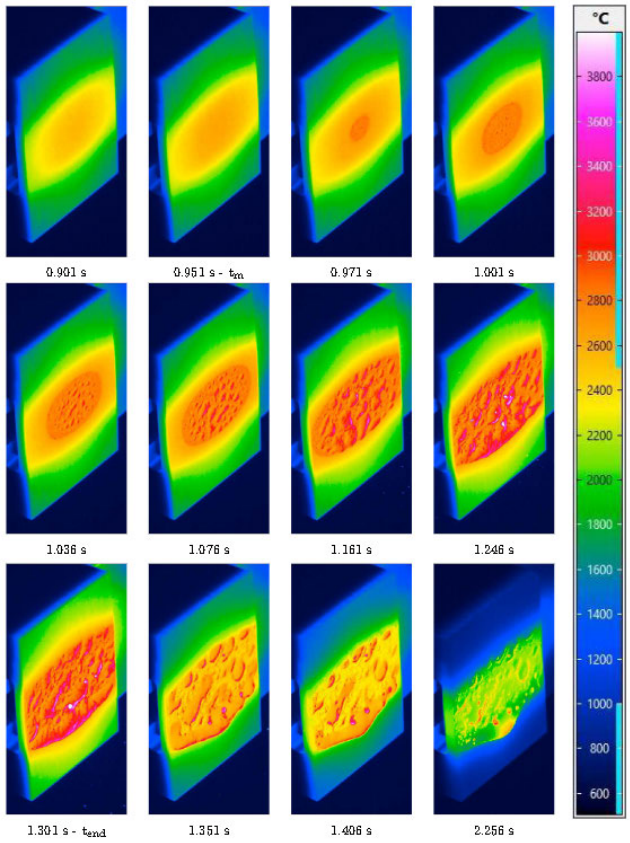

Fig. 6. TZM-2 IR frames showing the temperature and melt pool evolutions at different time instants during the heat pulse.

The gap in 2c-Pyro measurements is visible for the cyan curve of Fig. 7.

Figs. 7 and 8 show good agreement with experimental data, as far as the maximum temperature evolution and melt pool footprint is concerned. This is valid for the other samples as well. The quantitative benchmark will be discussed in Section IX.

B. W—Temperature Data, Imaging, and Benchmark

This section is dedicated to the results related to W samples. Fig. 9 collects the main IR frames during the pulse, whereas Fig. 10 shows measured and calculated temperature evolutions. Contour plots of temperature and melt pool are reported in Fig. 11.

C. SS—Temperature Data, Imaging, and Benchmark

This section reports the results related to SS samples. Fig. 12 collects the main IR frames during the pulse, whereas Fig. 13 shows measured and calculated temperature evolutions. Contour plots of temperature and melt pool are reported in Fig. 14.

VII. Mass Loss Estimate

Consideration on mass losses is here attempted, despite the difficulty of discerning between the different mechanisms enhancing them. For every sample, the experimental mass loss is calculated by comparing the weight measurements before

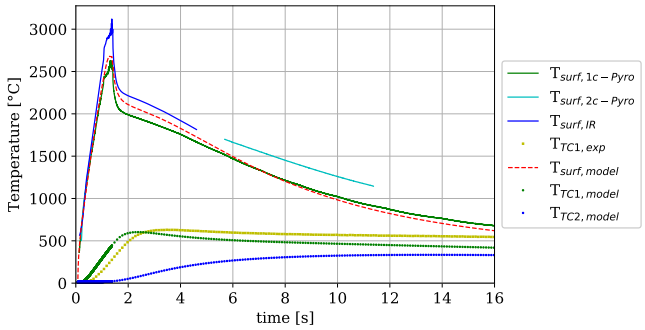

Fig. 7. TZM: thermal benchmark. The modeled data are labeled with the subscript *model*, while the experimental data are labeled with the subscript *exp*. The 2c-Pyro is insensitive for temperature measurements above 1700 °C, as the gap in the cyan curve shows.

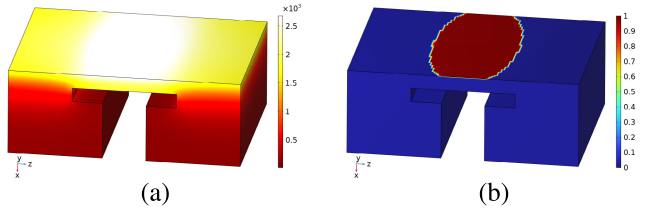

Fig. 8. TZM. (a) Temperature field [°C] and (b) related melt pool (Ω_2) at the end of the heating time, computed by 3-D TARTIFL&TTE.

and after the heat pulses. These measurements are reported in Table II, where the bigger difference in weight between the two W samples is due to the W-1 sample being manufactured slightly undersized. Table II also collects some of the 3-D TARTIFL&TTE outputs, i.e., the mass loss due to the

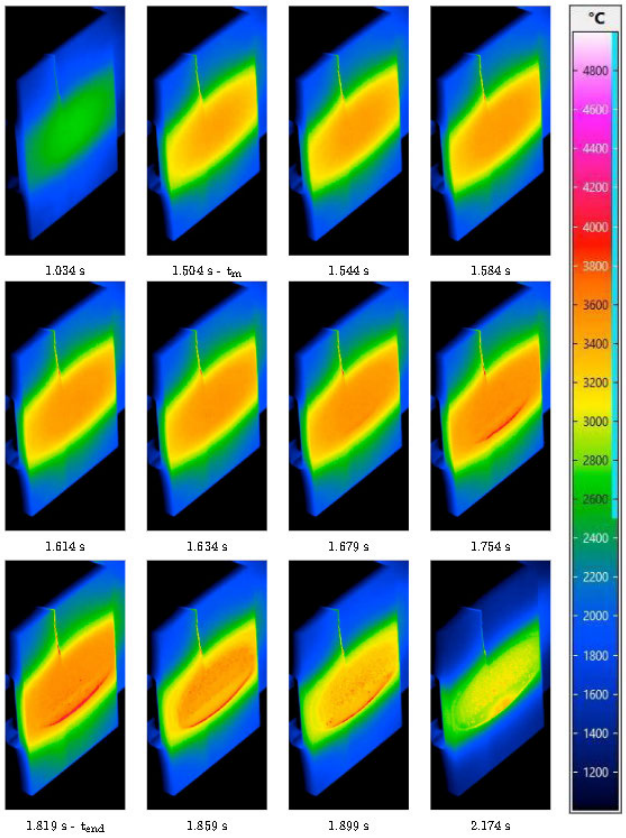

Fig. 9. W IR frames showing the temperature and melt pool evolutions at different time instants during the heat pulse.

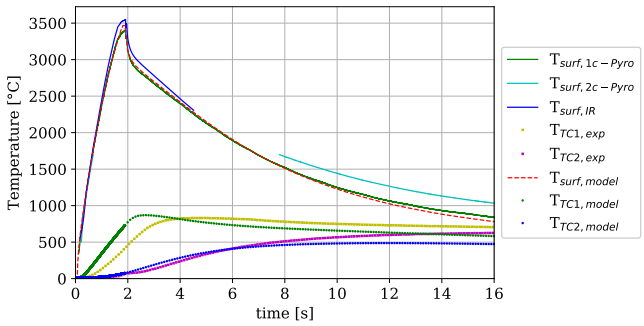

Fig. 10. W: thermal benchmark. The modeled data are labeled with the subscript *model*, while the experimental data are labeled with the subscript *exp*. The 2c-Pyro is insensitive for temperature measurements above 1700 °C, as the gap in the cyan curve shows.

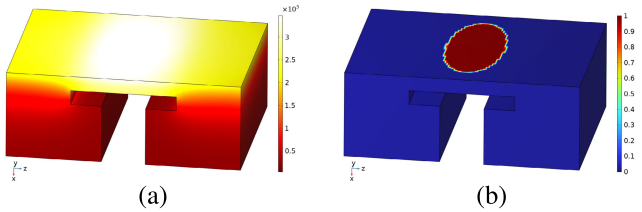

Fig. 11. W. (a) Temperature field [°C] and (b) related melt pool (Ω_2) at the end of the heating time, computed by 3-D TARTIFL&TTE.

evaporative mass flux departing from the surface and the total mass of liquid metal within the melt pool volume.

The experimental mass loss is neither matched by the evaporative mass loss nor the modeled total molten mass for none of the samples but the TZM-1, where the measured mass

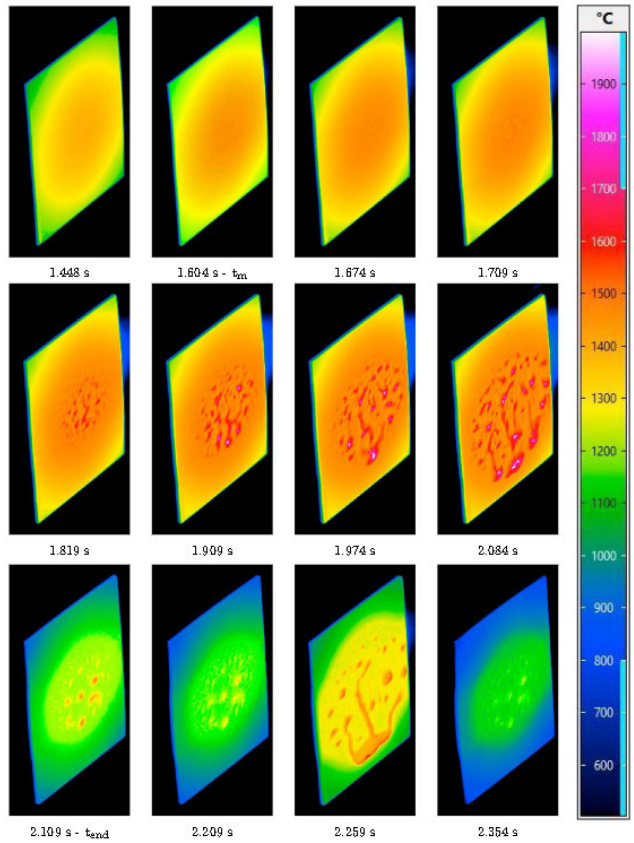

Fig. 12. SS IR frames showing the temperature and melt pool evolutions at different time instants during the heat pulse.

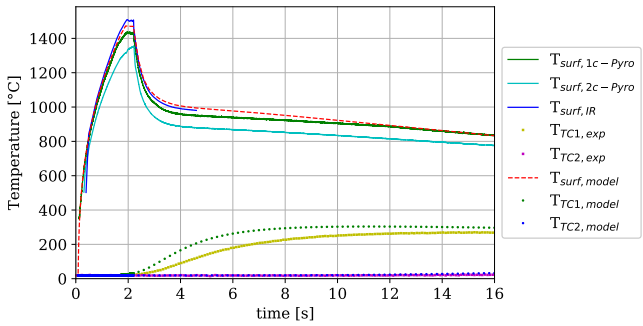

Fig. 13. SS: thermal benchmark. The modeled data are labeled with the subscript *model*, while the experimental data are labeled with the subscript *exp*.

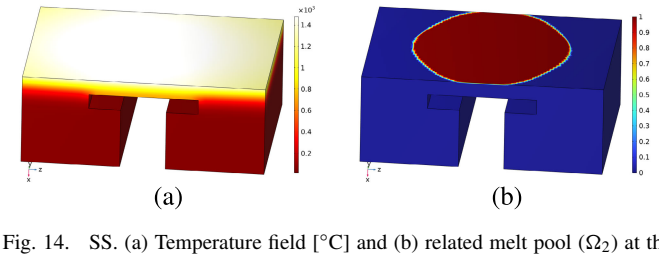

Fig. 14. SS. (a) Temperature field [°C] and (b) related melt pool (Ω_2) at the end of the heating time, computed by 3-D TARTIFL&TTE.

loss is closer to the total molten pool mass computed by the 3-D TARTIFL&TTE. This conclusion is also supported by the fact that the TZM-1 sample loses almost all the molten layer during the heat pulse, as highlighted in Fig. 5. For all the other samples, it is reasonable to assume that there are other mechanisms driving the melt mass loss, as the stepwise

TABLE II
SAMPLES' MASS LOSSES BEFORE AND AFTER THE EXPERIMENTS

Sample	Weight measurements [g]			3D-TARTIFL&TTE [g]	
	Pre-experiment	Post-experiment	Mass loss	Vapour mass	Molten mass
TZM-1	1090.53±0.3	1080.04±0.03	10.49±0.2	0.002	9.00
TZM-2	1089.17±0.04	1089.07±0.04	0.11±0.04	0.005	2.70
W-1	2123.57±0.03	2123.48±0.03	0.09±0.03	0.001	3.19
W-2	2136.49±0.03	2136.36±0.03	0.13±0.03	0.001	2.06
SS-1	891.15±0.04	891.10±0.04	0.05±0.04	0.00071	1.48
SS-2	889.70±0.04	889.66±0.04	0.03±0.04	0.0017	3.50

heat pulse duration calibration aims at reducing the liquid mass losses under gravity, and the evaporative mass flux is not enough for justifying the experimental mass loss.

VIII. MELT LAYER DEPTH RESULTS FROM DESTRUCTIVE POSTPROCESSING

A destructive postprocessing is pursued at the end of the experimental campaign, aiming to sectioning the samples for morphology investigations. The detection of the interface position between different microscopic crystalline domains should provide indication on the molten layer depth at the end of the transient.

This involves the extraction of the two vertical and horizontal specimens highlighted in green and red, respectively, as shown in Fig. 15(a) and (b). The cut in Fig. 15(c) separates the loaded volume from the T-legs, thus providing the surface in black in Fig. 15(c), taken as reference for measurements. The aim is to identify, across each specimen's thickness, any alteration in the metallic crystalline morphology caused by phase transition, and correlate the depth of the molten layer with any visible physical interface between areas with different morphologies. The thickness of the molten layer is retrieved by averaging the three lowest measurements of the thickness of the unmelted material, from the reference point up to the top surface, and subtracting this value from the original thickness (5 mm) of the loaded volume in violet in Fig. 15(c). Where it is not possible to identify any interface, the lowest point measured beneath the footprint is considered as the interface between solid and liquid phases. The maximum depth values are then benchmarked against the computational results from the 3-D TARTIFL&TTE.

A data summary of both the experimental and modeled molten thickness estimates is reported in Table III, which highlights that the depth of the melt pool is matched in its order of magnitude for all the samples. In the following, considerations on the sample's cross sections clarify the novel experimental methodology followed for melt layer depth measurements.

The most representative cross sections of TZM, W, and SS specimens are shown in Figs. 16–18, respectively. As far as TZM is concerned, the horizontal specimens are mainly characterized by recrystallized grains of similar size (hundreds of micrometers), without elongated columnar growth beneath the loaded area. On the contrary, the vertical specimen in Fig. 16 shows grains consistently elongated with the direction of the heat flux, reaching up to 500 μm below the loaded area, with less porosity that the recrystallized structure beneath them. The pink cross marks draw a separation line between solidified molten layer and recrystallized structure, whereas the green marks identify a second interface separating this

TABLE III
MOLTEN THICKNESS ESTIMATE BENCHMARK SUMMARY

Sample	Experimental [m]	3D-TARTIFL&TTE [m]
TZM-1	1.74E-03 ± 1.5E-05	1.00E-03
TZM-2	7.33E-04 ± 2.4E-05	2.62E-04
W-1	7.54E-04 ± 1.2E-05	2.31E-04
W-2	7.54E-04 ± 1.2E-05	2.31E-04
SS-1	1.38E-04 ± 2.4E-05	2.31E-04
SS-2	1.83E-04 ± 7E-06	2.71E-04

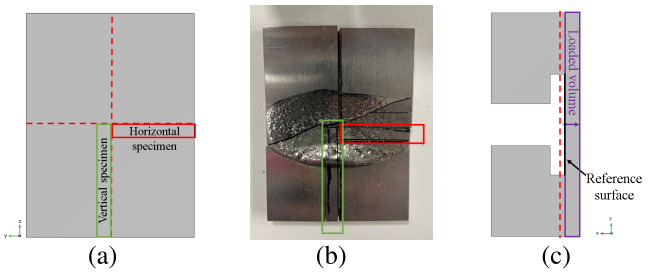

Fig. 15. (a) Top view of the sample sectioning in four parts (red lines), highlighting the vertical (green) and horizontal (red) specimens. (b) Real sample sectioning. (c) Lateral view of the loaded volume, whose surface in black is taken as reference for measuring the unmelted layer.

last region from the original bulk structure, characterized by grain size of tens of micrometers. Although the TZM shows a bulk porous structure, bigger size voids are trapped closer to the surface, breaking the continuity of the molten layer, where visible. The bigger voids close to the surface may be originated by coalescence of smaller voids, migrating to the surface and bursting under the beam heat flux.

W has a similar melting behavior than TZM. Although two specimens are lost due to a bad cut slicing off the reference surface, the other two specimens show an elongated crystal growth beneath the heated area, and the direction of this growth is parallel to the beam source that mainly dictates the preferred direction of the heat transfer across the sample during the heat pulse. This is visible in both the vertical and horizontal specimens, as opposed to TZM, and it is identified in Fig. 17, where the crystal growth can form conglomerates of hundreds of microns from pre-existing grains. The structure below the melted interface has grain size of around 70 μm, although the vertical specimen shows the existence of a third smaller grain domain, which is probably the original W bulk structure with grains not bigger than 50 μm. The difference in grain size for W enables the authors to draw a physical interface between grain growth closer to the heated surface and the pentagonal grain shape throughout the specimen. The bulk of the structure is instead recrystallized under heat treatment, and this prompts the grains to minimize their exposed area to keep the lowest energy level at the boundary. In addition to grain growth and recrystallization, it is important to highlight the void-like structures remarking the interface between the resolidified and bulk microstructure. Both the W specimens show smaller lined-up bubble-like structures at the solid-to-liquid interface, which become bigger in size as they approach the melt wobbling surface. The smaller voids probably appears once the melting starts, and coalesce throughout the duration of the heat pulse before the molten layer drifts. Local evaporation and bubble bursting affects the size and shape of these

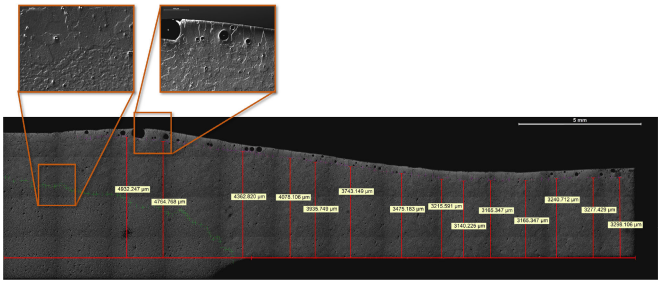

Fig. 16. TZM specimen morphology.

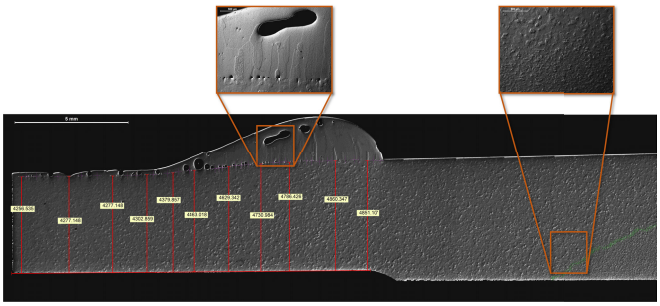

Fig. 17. W specimen morphology.

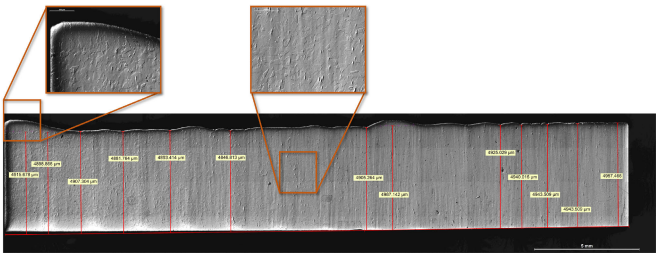

Fig. 18. SS specimen morphology.

voids. The biggest visible bubble within the resolidified droplet in Fig. 17 shows the coalescence of bubbles trapped within the molten layer on their way to the surface. The same bubbly phenomenon is observed in W sample molten layers analyzed in [4] and [5]. It cannot be excluded that H and other gaseous content affects the bubble formation and growth. Both TZM and W vertical specimens show the melt droplet drifting down under gravity.

Similar to the W sample, most of the SS specimens are discarded because the reference surface is not preserved during the sectioning. However, for the ones only partially showing the reference surface, it is possible carrying on with the measurements by setting a new reference line built upon the visible reference surface. The tiled images of the horizontal SS specimen is shown in Fig. 18. This is representative of all the SS specimens, showing a wobbling exposed surface, with bumps characterized by a dendrite structure with thinner elongated grains, which differ from the bulk.

IX. Results and Discussion

The quantitative benchmark of the cases analyzed in Section VI is summarized in Table IV, which supports the following general conclusions.

Starting from the integrated energy density, both model and experiments agree very well, except for the SS samples where an increase of 7% in the heat flux peak is necessary to match the experimentally measured absorbed energy. Problems of sample assembly and cooling are of minor significance as the short pulse loading is adiabatic. The deviation of the SS samples could be explained with difficulties of optical temperature measurements on steel surfaces at low emissivity, combined with uncertainties in the SS-316 thermophysical properties. Considering the 7% heat flux increase for SS samples, it follows a good prediction of the maximum surface temperature collected by the 1c-Pyro for all the samples, whose agreement is well within 1%–3%. IR temperature values are higher than the ones captured by Pyro; therefore, the discrepancy between the IR values and the modeled $T_{\max}$ is within 2%–14%.

The melting phase is triggered by 3-D TARTIFL&TTE a fraction of seconds after the melting time detected by the diagnostics, with a 12%–18% delay with respect to the experimental data. To some extent, this depends on the T_m value triggering the melting phase. Furthermore, 3-D TARTIFL&TTE predicts the maximum temperature value measured by TC1 within 21%, whereas the agreement with the TC2 data is within 25% for all the heat pulses apart from the TZM-1 one. In this case, the maximum modeled temperature is half the experimental value. It cannot be excluded that the TC2 gets damaged during the first TZM-1 heat pulse, as the same TC fails during the TZM-2 heat pulse. It is difficult to accurately explain this mismatch, besides that the 3-D TARTIFL&TTE models the TC measurements through a probe located in place of the TC holes with neither contact resistance nor other factors affecting the experimental TC measurements to be considered.

Unlike TZM and SS, both the W samples experience cracking damage as soon as they start heating up. This is due to the brittle behavior of W at temperatures below ≈800 °C. However, the cracks do not affect the experiments as they do not cause the tile to fall apart over the entire duration of the heat pulse. The investigation of the cracking damage is not part of this study.

As far as the molten thickness benchmark in Section 2 is concerned, the following considerations can be derived from Table III. Both the experimental measurements and the 3-D TARTIFL&TTE estimates target the same order of magnitude of the molten thickness, despite the difference in modules. As far as TZM and W are concerned, 3-D TARTIFL&TTE underestimates the module of the melt pool thickness compared with the experimental one, and the closest prediction achieved for the TZM-1 is within 36%. This difference increases up to 70% for TZM-2 and W samples. The TZM-1 loses almost all the liquid mass during the heat pulse under the effect of gravity and splashes of liquid droplets, as it is the first loaded sample experiencing a longer loading time than the others. Furthermore, TZM-1 is the only sample where the computed molten mass agrees within 15% with the measured sample weight loss (see Section 2), if it is assumed that the total mass of the calculated melt pool volume is removed from the computational domain. Considering this, it can be concluded that the TZM-1 sample loses almost all the molten mass under gravity acting over the heat pulse, whose little remainder solidifies on the surface. For all the other samples, the measurement of the mass losses does

TABLE IV
THERMAL BENCHMARK RESULT SUMMARY

		TZM-1/TZM-2			W-1/W-2			SS-1/SS-2		
		Exp	Model	Δ[%]	Exp	Model	Δ [%]	Exp	Model	Δ [%]
HF_{max} [MW m^{-2}]		30		–	30		–	10	10.7	7%
Δt [s]		1.57/1.30		–	1.87/1.82		–	1.88/2.11		–
E_{abs} [kJ m^{-2}]		206/171	205/170	0%/0%	245/239	244/238	0%/0%	87/98	87/98	0%/0%
T_0 [°C]		12/13		–	12/17		–	20/19		–
t_m [s]	IR	0.96/0.95	1.11	16%/17%	1.49/1.5	1.68	14%/13%	1.61/1.60	1.64	2%/2%
	1c-Pyro	0.96/0.95		16%/17%	1.48/1.5		14%/13%	1.61/1.63		2%/0%
T_{max} [°C]	IR	3024/3120	2911/2680	4% / 14%	3591/3548	3473/3468	3%/2%	1504/1509	1473/1473	2%/2%
	1c-Pyro	2859/2631		2%/2%	3433/3401		1%/2%	1440/1437		2%/3%
	TC1	731/627	700/603	4% / 4%	768/830	893/870	16%/5%	227/270	275/303	21%/12%
	TC2	570/NA	277/334	50%/NA	598/628	496/487	17%/22%	66/43	61/32	6%/24%

not match neither the evaporative mass loss nor the total amount of mass within the melt pool volume. This brings the authors to think that the latter samples are instead characterized by evaporative losses plus a partial loss of molten mass, which is difficult to accurately isolate and quantify. Therefore, the mechanisms behind the liquid mass losses need to be investigated in the future, as they constitute one of the big uncertainties. The only mass lost from the 3-D TARTIFL&TTE computational domain is the evaporative mass flux, as opposed to the experimental mass loss affected by both gravity and splashes of liquid droplets under the beam impact. For this reason, there is no match between the experimental mass loss computed by weighting the samples before and after the experiments, and the calculated value (neither in terms of evaporative mass loss nor total amount of liquid mass).

A different conclusion can be stated for the SS samples, for which 3-D TARTIFL&TTE predicts a deeper melt pool with a higher mean value than the experimental measurements. This might be caused by the increase in heat flux for matching the absorbed energy density value.

Overall, the main achievement of this comparison is matching the predicted melt pool depth in its order of magnitude by means of a novel approach. The comparison suggests that the methodology works, despite the module discrepancies. These can be driven by uncertainties affecting the experimental process, which starts from a more accurate sample metrology assessment before and after the experiments. Furthermore, the postmortem analyses require more accurate cross sectioning of the samples, for which it is important to preserve any reference surface unaltered during any sectioning.

X. CONCLUSION

The benchmark of the 3-D TARTIFL&TTE results against dedicated melting experimental data supports the authors' approach to phase transition modeling. The following points are highlighted.

1) A good agreement on surface temperature and absorbed energy.
2) A good agreement on molten layer thickness despite the discrepancy between TARTIFL&TTE assumptions and gravity action, as well as experimental uncertainties.

ACKNOWLEDGMENT

The authors acknowledge the crucial support from: 1) UKAEA STEP Project for providing the samples; 2) EUROfusion for granting access to the GLADIS Facility; 3) UKAEA Materials Research Facility supporting the destructive post-processing and granting access to the Non-Active Sample Prep Laboratory; and 4) Oxford Materials Characterisation Service, Department of Materials, University of Oxford, Begbroke Science Park, for granting access to their Laboratories and optical equipment needed for the destructive postprocessing.

Views and opinions expressed are, however, those of the author(s) only and do not necessarily reflect those of the European Union or the European Commission. Neither the European Union nor the European Commission can be held responsible for them.

REFERENCES

[1] M. L. Richiusa, P. Ireland, J. Nicholas, and Z. Vizvary, "Rationale behind EU-DEMO limiter's plasma-facing component design under material phase change," *IEEE Trans. Plasma Sci.*, vol. 50, no. 11, pp. 4226–4232, Nov. 2022.

[2] M. L. Richiusa, P. Ireland, F. Maviglia, J. Nicholas, and Z. Vizvary, "Advances in material phase change modelling approach for EU-DEMO limiter's plasma-facing components," *Fusion Eng. Design*, vol. 189, Apr. 2023, Art. no. 113477.

[3] H. Greuner et al., "Design, performance and construction of a 2 MW ion beam test facility for plasma facing components," *Fusion Eng. Design*, vol. 75, no. 79, pp. 345–350, Nov. 2005.

[4] J. W. Coenen et al., "Analysis of structural changes and high-heat-flux tests on pre-damaged tungsten from tokamak melt experiments," *Phys. Scripta*, vol. T145, Dec. 2011, Art. no. 014066.

[5] J. W. Coenen et al., "Tungsten melt layer motion and splashing on castellated tungsten surfaces at the tokamak TEXTOR," *J. Nucl. Mater.*, vol. 415, no. 1, pp. S78–S82, Aug. 2011.